PAPER • OPEN ACCESS

First observation of edge impurity behavior with n = 1 RMP application in EAST L-mode plasma

To cite this article: Wenmin Zhang *et al* 2024 *Nucl. Fusion* **64** 086004

OPEN ACCESS
IOP Publishing | International Atomic Energy Agency
Nuclear Fusion
Nucl. Fusion **64** (2024) 086004 (13pp)
https://doi.org/10.1088/1741-4326/ad4ef4

First observation of edge impurity behavior with $n = 1$ RMP application in EAST L-mode plasma

Wenmin Zhang[1,2], Ling Zhang[1,*], Yunxin Cheng[1], Shigeru Morita[3], Hui Sheng[1], Darío Mitnik[4], Youwen Sun[1], Zhengxiong Wang[5], Yuqi Chu[6], Ailan Hu[1], Yinxian Jie[1,*] and Haiqing Liu[1]

[1] Institute of Plasma Physics, Hefei Institutes of Physical Science. Chinese Academy of Sciences, Hefei 230031, China
[2] University of Science and Technology of China, Hefei 230026, China
[3] National Institute for Fusion Science, Toki 509-5292, Gifu, Japan
[4] Instituto de Astronomía y Física del Espacio (CONICET-Universidad de Buenos Aires), Buenos Aires 1428, Argentina
[5] Dalian University of Technology, Dalian 116024, China
[6] University of California Los Angeles, Los Angeles, CA 90095, United States of America

E-mail: zhangling@ipp.ac.cn and yx_jie@ipp.ac.cn

Received 14 January 2024, revised 18 April 2024
Accepted for publication 22 May 2024
Published 18 June 2024

Abstract

High-Z impurity accumulation suppression and mitigation in core plasma is frequently observed in EAST edge localized mode mitigation experiments by using resonant magnetic perturbations (RMP) coils. To study the individual effects of the RMP field on impurity transport, based on high-performance extreme ultraviolet impurity spectroscopic diagnostics, the effect of the $n = 1$ (n is the toroidal mode number) RMP field on the behavior of intrinsic impurity ions at the plasma edge, e.g. He^{+}, Li^{2+}, C^{2+}–C^{5+}, O^{5+}, Fe^{8+}, Fe^{15+}, Fe^{17+}, Fe^{22+}, Cu^{17+}, Mo^{12+}, Mo^{13+} and W^{27+}, is analyzed for the first time in L-mode discharges. Based on the evaluation of the location of these impurity ions, it is found that with the increase in RMP current (I_{RMP}), an impurity screening layer inside the last closed flux surface is formed, e.g. at $\rho = 0.74$–0.96, which is also the region that the RMP field affects. Outside this screening layer, the impurity ion flux of He^{+}, Li^{2+}, C^{2+}, C^{3+}, O^{5+}, Fe^{8+}, Mo^{12+} and Mo^{13+} ions increases gradually, while inside this screening layer, the impurity ion flux of C^{4+}, C^{5+}, Cu^{17+}, W^{27+}, Fe^{15+}, Fe^{17+} and Fe^{22+} ions decreases gradually. When I_{RMP} is higher than a threshold value, RMP field penetration occurs, accompanied with $m/n = 2/1$ mode locking, and the position of this screening layer moves to the plasma core region, i.e. $\rho = 0.66$–0.76, close to the $q = 2$ surface, and the opposite behavior of the impurity ion flux at two sides of the screening layer is strengthened dramatically. As a result, significant decontamination effects in the plasma core region, indicated by the factor of $((\Gamma_{Imp}{}^{Z+})_{w/o}-(\Gamma_{Imp}{}^{Z+}))/(\Gamma_{Imp}{}^{Z+})_{w/o}$ (where $(\Gamma_{Imp}{}^{Z+})/(\Gamma_{Imp}{}^{Z+})_{w/o}$ denotes the impurity ion flux ratio with and without RMP), is observed, i.e. 30%–60% for heavy impurity (Fe, Cu, Mo, W), and ~27% for light impurity of C. In addition, the analysis of the decontamination effects of C and Fe impurities under four

* Authors to whom any correspondence should be addressed.

different RMP phase configurations shows that it may be related to the strength of the response of the plasma to RMP. These results enhance the understanding of impurity accumulation suppression by the $n = 1$ RMP field and demonstrate a candidate approach using RMP coils for W control in magnetic confinement devices.

Keywords: EAST tokamak, impurity ion flux, resonant magnetic perturbations, screening layer

(Some figures may appear in colour only in the online journal)

1. Introduction

In current and future fusion devices, materials with high atomic numbers are used as plasma-facing components (PFCs) due to positive characteristics, i.e. high melting point, low sputtering yield and low tritium retention [1, 2]. However, impurities are inevitably introduced due to plasma–material interactions in discharges. The presence of these impurities, especially high-Z impurities (Mo and W), which are never completely ionized in fusion devices, enhances the energy loss through high radiation capability [3]. These effects lead to degradation of the confinement properties of the plasma, or even termination of the discharge [4, 5]. Therefore, it is essential to study and effectively control the source of these impurities in the PFCs and its transport in the scrape-off layer (SOL) and the confined plasma [6]. At present, the main methods for reducing impurity concentration in magnetic confinement devices typically involve the following. Firstly, the device wall is cleaned prior to discharge to remove the impurity particles attached to the wall [7]. Secondly, low-Z material wall coating and real-time injection of Li and B granules are performed before or during experiments to adsorb and neutralize the impurity and reduce edge fuel recycling [8–12]. Thirdly, on-axis radio-frequency (RF) wave heating, including electron cyclotron resonance heating (ECRH) [13–15], lower hybrid wave (LHW) [16] and ion cyclotron resonance heating (ICRH) [17, 18], is used to effectively mitigate impurity accumulation. In addition, magnetohydrodynamic (MHD) activity in the plasma, e.g. the sawtooth instability and edge localized mode (ELM), can effectively eliminate impurities from the plasma core region [19, 20].

In recent magnetic confinement experiments, it has been found that the formation of an edge stochastic magnetic field, caused by an ergodic magnetic limiter (EML) [21], an ergodic divertor (ED) [22], a dynamic ergodic divertor (DED) [23] and resonant magnetic perturbation (RMP) coils installed in magnetic confinement fusion devices [24–28], has also proved to be an effective method to reduce impurity concentrations in the core region of confined plasmas. Previous studies of intrinsic C and O impurities on TEXT plasma have shown that the utilization of the EML can significantly enhance the particle diffusivity in the edge region of plasma, leading to a 20% reduction in low-Z impurities in the core of the plasma [21]. Similar experimental results were observed on Tore Supra using the ED configuration and TEXTOR operating in $m/n = 3/1$ (here, m is the polarity mode number, and n is the toroidal mode number) DED mode. Specifically, the screening effect of the ergodic layer resulted in a significant reduction in the impurity content of the confined plasma due to effective reduction of the edge impurity confinement time (i.e. an increased peripheral recycling flux) in Tore Supra plasma [29]. In TEXTOR plasma, decontamination of highly ionized C ions (C^{4+} and C^{5+}) can be explained in terms of plasma flow along magnetic field lines and frictional forces [30]. In recent years, experimental results on RMP ELM control in DIII-D and EAST have demonstrated effective impurity exhaust during ELM suppression and mitigation [31, 32], with a clear reduction in the impurity concentration in core plasma, and the effect is found to be stronger for lower n ($n = 1, 2$) compared to higher n ($n = 3, 4$) in EAST [33]. In addition, the results from LHD and TEXTOR demonstrated that the induced magnetic island by the RMP field in the plasma edge can enhance He ash exhaust from the device by reducing the effective He confinement time [34]. Simultaneously, investigations in DIII-D provide evidence that future magnetically confined devices applying RMP ELM suppression may meet or even exceed the He exhaust provided by the ELMs themselves [35]. Furthermore, experiments on DIII-D have demonstrated that RMP reduces the impurity confinement time in the H-mode pedestal below that of natural ELM plasmas, indicating that RMP fields are beneficial for controlling the buildup of impurities in the pedestal region of the plasma [31]. However, the physical mechanism underlying the impact of RMP on impurity transport in magnetically confined devices remains unclear. Mitigation and suppression of type-I ELM has been realized in H-mode discharges dominated by pure RF and neutral beam injection (NBI) heating in EAST plasma [27, 32, 36]. Meanwhile, the impurity concentration in the core plasma region is obviously reduced. This may be due to reduced impurity source generation during the application of RMP, offering effective mitigation of transient heat and particle flux loads on the PFCs [37]. Meanwhile, the edge magnetic topology induced by RMP also improves impurity screening effects in the edge region [38]. However, it is difficult to isolate the effects of the RMP field and ELM activity on impurity transport behavior in H-mode discharges. Therefore, based on the temporal evolution and spatial distribution observation of impurity line emission from intrinsic low-Z (He, Li, O, C), medium-Z (Fe, Cu) and high-Z (Mo, W) ions with different ionization stages [39–46], the effects of RMP on the impurity transport in LHW heated L-mode discharges are studied for the first time in EAST.

This paper is organized as follows. The experimental setup and the high-performance extreme ultraviolet (EUV) impurity spectroscopic diagnostics system are introduced in section 2.

The impact of RMP on the impurity behavior in EAST experiments is presented in section 3. The RMP effect on the impurity behavior is discussed in section 4, followed by a summary in section 5.

2. Experimental setup

After the recent upgrade in EAST, the upper and lower divertor have been upgraded to be W divertors; the first wall is mainly composed of Mo tiles, and the diagnostic protection shield, radio frequency wave antennas and limiter are mainly Fe, Cu and W materials. Graphite material is still used on the high-field side first wall at ports A and D, where an NBI system is installed. Additionally, several other low-Z impurity species exist in EAST plasma intrinsically, e.g. He and Li originating from glow discharge and wall treatment with a Li coating, while O is derived from adsorption on the main vacuum chamber wall in the atmosphere [9, 43]. The total current drive and heating source power, including NBI, ICRH, ECRH and LHW, have now exceeded 20 MW. Therefore, control of the medium-Z (Fe and Cu) and high-Z (Mo and W) impurity accumulation, especially W impurities, is one of the key issues for sustaining long-pulse high-performance steady-state operation in EAST [47]. In addition to on-axis ECRH and LHW, RMP is one effective method for mitigation impurity accumulation in the central region of the plasma.

A set of in-vessel flexible RMP coil systems for MHD control and related three-dimensional physics research were installed in EAST in 2014 [27]. The EAST vacuum vessel consists toroidally of 16 ports, named as capital letters from A to P counterclockwise from the top view. The mid-plane A port points to the north direction. There, the RMP coil system consists of two arrays of coils with up and down symmetry located in the upper (U) and lower (L) parts of the last closed flux surface in the low-field side. Each coil has four turns and covers two ports. The absolute zero degree of the toroidal angle, Φ, is defined as the location at the center of the first coil (U1 or L1), and $\Delta\Phi_{\rm UL} = \Phi_{\rm U} - \Phi_{\rm L}$ is the phase difference between upper and lower coils. The RMP spectrum can be adjusted by changing the upper–lower coil phasing. The toroidal mode number, n, of the RMP generated by the coil system can be up to $n = 4$ for static perturbation and $n = 3$ for rotating ones. For a high toroidal mode of $n = 3$, 4 cases, the perturbation field is mainly located in the plasma edge region compared with the low $n = 1$, 2, which has less impact on the plasma confinement performance. Furthermore, both DC and AC currents can be produced, and connection parity could be changed between odd (opposite-phase current waveform in the upper and lower rows of coils) and even modes because every two coils with 180° toroidal separation in each array are paired with a switch.

Recently, the observation capability of lowly ionized impurity ions at the plasma edge in the EAST device has been largely enhanced by two newly developed sets of 5 ms/frame fast-time-response EUV spectrometers (called EUV_Long_b, and EUV_Long_c) working at 20–500 Å (scannable). The lines of sight (LOS) for these two fast-time-response EUV spectrometers primarily cross through the plasma edge region, as shown in figure 1. By combining with the previously developed two spectrometers, whose LOS mainly pass through the plasma central region (EUV_Short and EUV_Long_a) [39, 41], where the LOS is shown in figure 1, simultaneous observation of lowly–highly ionized low-, medium- and high-Z impurity ions becomes possible, and the capability for study of the edge–core coupling impurity transport is enhanced. In addition, a pair of space-response EUV spectrometers (called EUV_Long2_u and EUV_Long2_d), working at 30–520 Å (scannable) with different radial observation ranges of -6 cm $\leqslant Z \leqslant$ 44 cm and -40 cm $\leqslant Z \leqslant$ 10 cm at $R = 1.9$ m, have been upgraded to extend the radial profile observation range ($\rho \leqslant 0.7$) of the impurity line emission [40, 45]. The vertical observation range is also indicated in figure 1. Therefore, it is effective to monitor the density distribution of intrinsic impurity ions and their spatiotemporal evolution behavior based on the EUV impurity spectroscopic system, and to investigate transport in the SOL and bulk plasma. For the discharges studied in this work, the fast-time-response EUV spectrometers EUV_Short, EUV_Long_a, EUV_Long_b and EUV_Long_c, are operated at 5–50 Å, 40–180 Å, 245–500 Å and 160–385 Å, respectively. The space-resolved EUV spectrometers are operated at 45–75 Å, 65–100 Å and 100–140 Å in three repeated discharges, respectively. In addition, absolute intensity calibration has been performed on all the EUV spectrometers.

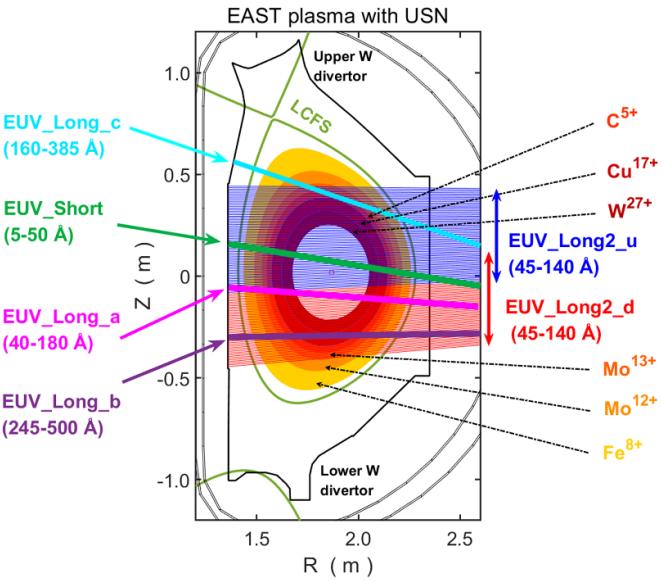

Figure 1. The LOS of two pairs of space-resolved EUV spectrometers: EUV_Long2_u (light blue lines) and EUV_Long2_d (light red lines), and four fast-time-response EUV spectrometers: EUV_Short (green line), EUV_Long_a (magenta line), EUV_Long_c (cyan line) and EUV_Long_b (purple line). Six shaded areas with gradient colors from orange to red indicate the estimated distribution region of particular impurity ions of Fe^{8+} (151–234 eV), Mo^{12+} (230–279 eV), Mo^{13+} (279–302 eV), C^{5+} (392–490 eV), Cu^{17+} (552–632 eV) and W^{27+} (833–881 eV) in EAST L-mode discharge at $T_{e0} = 1.8$ keV. The edge poloidal plasma cross section denoted by a dark-green solid line indicates the upper single-null (USN) divertor configuration of the EAST tokamak.

The radial profiles of electron density (n_e) are measured by a polarimeter interferometer (POINT) [48], and radial profiles of electron temperature (T_e) are provided by a Thomson scattering (TS) diagnostic and 32-channel heterodyne radiometer system of electron cyclotron emission (ECE) [49]. Radiation power losses are measured by fast-response bolometers (AXUV) [50]. The effective charge (Z_{eff}) and density fluctuation are measured using a visible bremsstrahlung diagnostic and reflectometry [51, 52], respectively.

3. Effect of RMP on impurities' behavior in L-mode discharges

3.1. Time behavior

As a typical RMP current (I_{RMP}) ramp-up experiment, discharge #113745 is shown in figure 2, where the time interval during the flat top of the plasma current is displayed. The plasma current is $I_p = 0.45$ MA, the toroidal magnetic field is $B_T = -2.5$ T in the clockwise direction from the top view, the safety factor at the surface with 95% of the normalized poloidal flux, $q_{95} = 5.2$, and the central line-averaged density is sustained at $n_e = 3 \times 10^{19}$ m^{-3} by density feedback control with supersonic molecular beam injection (SMBI). The LHW power of $P_{LHW} = 1.0$ MW at 4.6 GHz and an ICRH power of 0.48 MW is injected during $t = 1.0$–7.4 s and $t = 2.2$–6.1 s, respectively (see figure 2(*a*)), in which the injection of ICRF power helps to increase the impurity level in this L-mode discharge [53]. The I_{RMP} is switched on at $t = 3.0$ s in the $n = 1$ DC mode with even parity; it is then controlled to slowly ramp up from 1.5 kA to 3.6 kA during $t = 3.0$–5.0 s (see figure 2(*b*)), and it is sustained at 3.6 kA during $t = 5.0$–5.5 s) and then switched off at $t = 5.5$ s. When the I_{RMP} gradually ramp ups from 1.5 kA to 3.6 kA during $t = 3.0$–4.8 s, there is almost no significant change in the B_r ($n = 1$ radial magnetic response perturbations), while the normalized intensity of the core AXUV signal I_{AXUV} slowly decreases. When I_{RMP} reaches 3.4 kA at $t = 4.8$ s, a sudden increase in the locked mode (LM) signal B_r ($n = 1$) is observed (see figure 2(*c*)), indicating field penetration or mode penetration and, simultaneously, a large LM stimulation occurs. Subsequently, the core I_{AXUV} drop obviously until I_{RMP} is switched off, as shown in figure 2(*e*). When I_{RMP} is switched off, the Mirnov signal in figure 2(*d*) suddenly increases, indicating that LM is unlocked. The structure of the excited mode is $m/n = 2/1$ based on mode analysis, which is the major resonant component of the applied RMP field [54]. Once the island unlocks, the core I_{AXUV} begin to recover beyond their original values, as shown in figure 2(*e*). In addition, during the application of the RMP field, it is found that Z_{eff} increases slowly, and when the RMP field penetrates, Z_{eff} increases significantly. Figure 2(*g*) shows the temporal evolution of the power spectrum of the density fluctuations measured by reflectometry [52]. Before RMP penetration, the low-frequency turbulence in the plasma core is enhanced with the increase in I_{RMP}, compared with $t = 5.8$ s after RMP is turned off, indicating that the enhancement of low-frequency turbulence may be conducive to impurity removal. However,

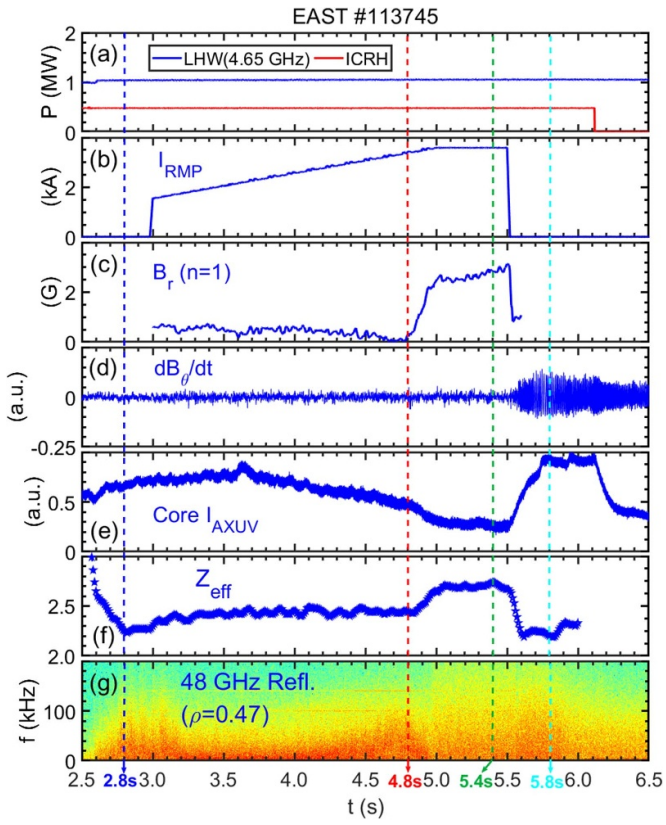

Figure 2. Time evolution during EAST L-mode discharge of (*a*) heating power of the LHW at 4.65 GHz (blue line) and ICRH (red line), (*b*) static $n = 1$ RMP coil currents, I_{RMP}, (*c*) $n = 1$ radial magnetic response perturbations, B_r, (*d*) the Mirnov signal, dB_θ/dt, (*e*) normalized radiation intensity along the chord passing through core plasma, core I_{AXUV}, and (*f*) the effective charge (Z_{eff}) measured by a visible bremsstrahlung diagnostic, and (*g*) density fluctuation measured by reflectometry. The timing at $t = 2.8$ s without RMP, $t = 4.8$ s at onset of RMP penetration, $t = 5.4$ s with $m/n = 2/1$ LM during field penetration, and $t = 5.8$ s with $m/n = 2/1$ tearing mode after RMP is switched off is indicated by vertical dashed lines in blue, red, green and cyan, respectively.

after $t = 4.8$ s RMP penetration, it is seen that the impurity radiation decreases more significantly with a wider broadband fluctuation.

Figures 3(*a*) and (*b*) show the radial profile of $R/L_{n_e} = -R\left(\mathrm{d}n_e/\mathrm{d}r\right)/n_e(R = 1.9\ \mathrm{m})$ and n_e measured by POINT, and T_e and $R/L_{T_e} = -R\left(\mathrm{d}T_e/\mathrm{d}r\right)/T_e$ measured by TS, respectively; here, polynomial fitting is applied to the T_e in figure 3(*b*), at four specific time points, represented by the vertical dashed lines in figure 2, which indicate the timing of $t = 2.8$ s without RMP (blue line), of $t = 4.8$ s at the onset of RMP penetration (red line), of $t = 5.4$ s with $m/n = 2/1$ LM during field penetration (green line), and of $t = 5.8$ s with $m/n = 2/1$ tearing mode (TM) after RMP is switched off (cyan line). It is found that the n_e is basically sustained due to SMBI density compensation, but there is difference in R/L_{ne}, as shown in figure 3(*a*). However, as shown in figure 3(*b*), with the RMP field application (see the red and green lines in figure 3(*b*)), the decrease in T_e can be observed, with T_{e0}

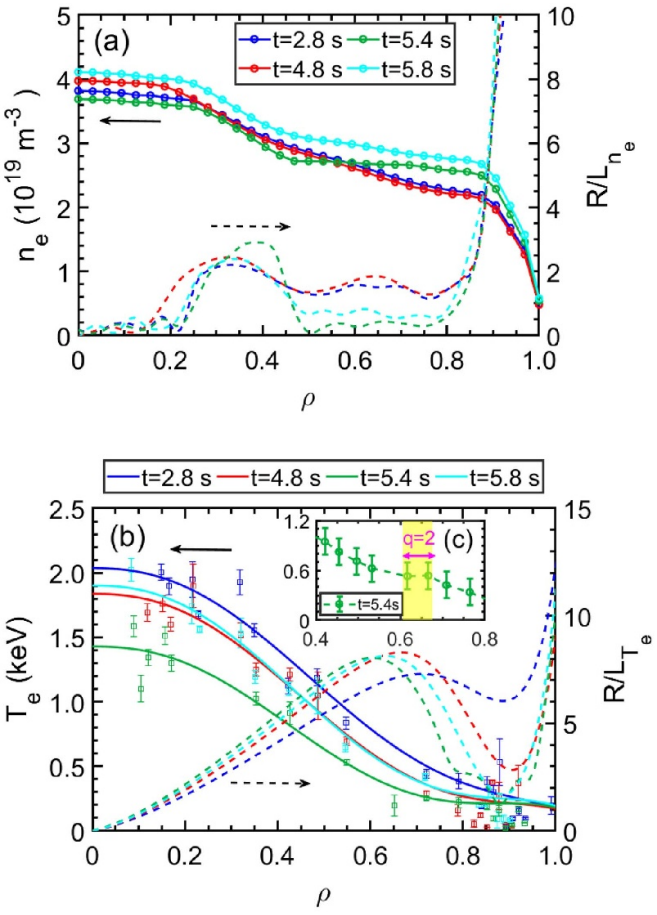

Figure 3. Radial profiles of (*a*) electron density and normalized electron density gradient scale length (R/L_{ne}, $R = 1.9$ m) measured by the POINT system, (*b*) the electron temperature and the normalized electron temperature gradient scale length (R/L_{Te}) measured by the TS system at four timings, and (*c*) the electron temperature profile from ECE zoomed in for $\rho = 0.4$–0.8 at $t = 5.4$ s in EAST discharge #113745.

decreasing by about 0.2 keV before RMP field penetration and about 0.5 keV after RMP field penetration. Once the RMP field is switched off, T_e begins to recover and returns to the level before RMP penetration (see the cyan line in figure 3(*b*)). It is observed from the radial profile of T_e measured by ECE in figure 3(*c*) that the magnetic island formed by RMP penetration on surface 2/1 causes a flattening of the T_e around the normalized radius $\rho \approx 0.61$–0.67, where the width of the magnetic islands can reach 5 cm and the uncertainty of the width of the magnetic island is less than 2 cm ($\Delta\rho < 0.025$), leading to a significant decrease in the T_e. The detailed determination of the width of the magnetic island can be found in [55]. However, there is no significant change in R/L_{Te}.

In figure 4, the yellow shaded area indicates that the I_{RMP} is slowly ramped up from 1.5 kA to 3.4 kA during the time period $t = 3.0$–4.8 s, while the green shaded area denotes that field penetration occurs while the I_{RMP} is continually ramped up from 3.4 to 3.6 kA, after which it remains at 3.6 kA during $t = 5.0$–5.5 s. Here, we present each impurity ion with the form of Imp^{Z+} ($E_i(Z-1) - E_i(Z)$), where Imp stands for the impurity species, Z is the ionization stage of the impurity ion, and $E_i(Z-1)$ and $E_i(Z)$ are the ionization energy required for previous and further ionization stages. During the application of RMP, there is a significant difference in the time-evolution behavior between the impurity ions in different radial locations since the RMP field alters the edge magnetic field topology. In this work, multiple emission lines emitted from different impurity ions with low to high ionization energy are chosen to study the local impurity transport change due to RMP field application, i.e. He^+ (24–54 eV) at 303.78 Å, Li^{2+} (75–122 eV) at 135 Å, O^{5+} (113–138 eV) at 173.095 Å, Fe^{8+} (151–234 eV) at 171.073 Å, Mo^{12+} (230–279 eV) at 340.909 Å, Mo^{13+} (279–302 eV) at 373.647 Å, C^{5+} (392–490 eV) at 33.734 Å, Cu^{17+} (552–632 eV) at 234.199 Å, and W^{27+} (833–881 eV) at 49.403 Å. Among them, the distribution regions of particular impurity ions of Fe^{8+}, Mo^{12+}, Mo^{13+}, C^{5+}, Cu^{17+} and W^{27+} are estimated at $T_{e0} = 1.8$ keV ($t = 4.8$ s), as shown in figure 1, with six shaded areas with gradient colors from orange to red. Since the impurity ion flux in the outermost area of the plasma confinement region can better indicate the impurity concentration in the confinement region, the flux of impurity ions entering the plasma region can be calculated. For a certain impurity element, A, the impurity influx for q-times ionized ion, A^{q+}, is calculated using $\Gamma_i = I_{obs} \cdot S/XB$ ($s^{-1} \cdot m^{-2}$) derived from the impurity transport equation [56], where Γ_i (ions $s^{-1} \cdot m^{-2}$) is the impurity influx, I_{obs} is the measured spectral line intensity (photons$\cdot s^{-1} \cdot m^{-2}$) from passive spectroscopy, S is the electron-impact ionization rate ($s^{-1} \cdot m^3$), X is the electron-impact excitation rate ($s^{-1} \cdot m^3$) and B is the branching ratio. The ratio coefficient S/XB is called the 'inverse photon efficiency', denoting the number of ionization events per observed photon (ions/photon). The S/XB values for He^+, Li^{2+}, O^{5+} and C^{5+} are taken from the ADAS database [57], while S/XB values for Fe^{8+}, Mo^{12+}, Mo^{13+}, Cu^{17+} and W^{27+} are calculated using the atomic structure computational codes HULLAC (Hebrew University—Lawrence Livermore Atomic Code) [58, 59]. As shown in figures 4(*b*)–(*e*), the time evolution of impurity ion flux is illustrated from edge to core with increasing ionization energy. When RMP is applied, it can also be observed that there is a significant or slight increase in all impurity fluxes ($t = 3$–3.3 s) due to the enhanced edge interaction caused by the instantaneous application of RMP. Moreover, the duration of the increase varies due to the different confinement and transport times of different impurity ions. During the I_{RMP} ramp up and before RMP field penetration ($t = 3.3$–4.8 s), the time behavior of impurity ion flux could be divided into two categories; one category presents a slightly increased tendency, i.e. for He^+, Li^{2+}, Fe^{8+}, Mo^{12+} and Mo^{13+} ions, which are located in more peripheral regions (see figures 4(*b*)–(*d*)). By contrast, another category presents a slightly decreased tendency, i.e. for C^{5+}, Cu^{17+} and W^{27+} ions, which are located in more core regions (see figures 4(*d*)–(e)), and the decreased tendency becomes stronger for the Cu^{17+} and W^{27+} ions located mostly in the core region. After RMP field penetration (from 4.8 s to 5.5 s), the time behavior of impurity ion flux can easily be divided into three categories. In the first category, the flux of He^+, Li^{2+} and O^{5+} significantly increases and sustains a saturated level

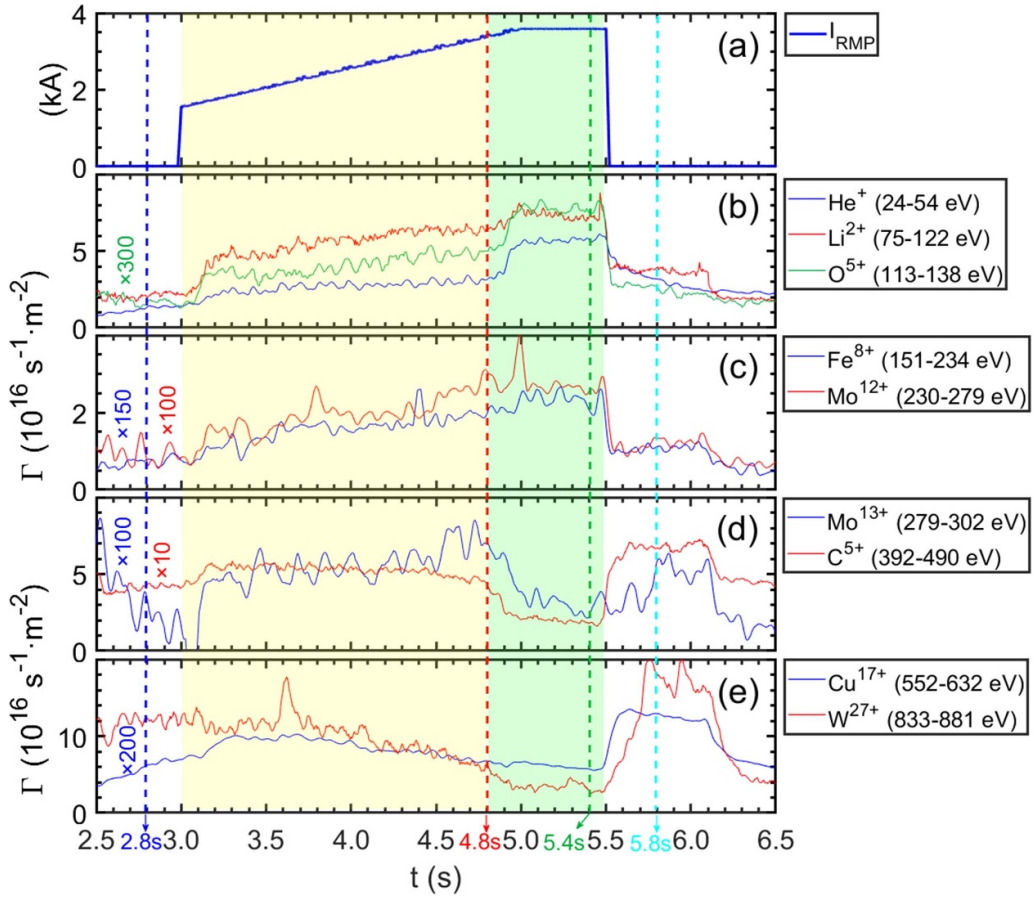

Figure 4. Temporal evolution of (*a*) static $n = 1$ RMP coil currents, and intrinsic impurity ion flux of (*b*) He^{+} (24–54 eV) at 303.78 Å, Li^{2+} (75–122 eV) at 135 Å and O^{5+} (113–138 eV) at 173.095 Å, (*c*) Fe^{8+} (151–234 eV) at 171.073 Å and Mo^{12+} (230–279 eV) at 340.909 Å, (*d*) Mo^{13+} (279–302 eV) at 373.647 Å and C^{5+} (392–490 eV) at 33.734 Å, and (*e*) Cu^{17+} (552–632 eV) at 234.199 Å and W^{27+} (833–881 eV) at 49.403 Å in EAST discharge #113745. The yellow shaded area indicates the time period before RMP penetration at $t = 3.0$–4.8 s, while the green one denotes the time period during RMP penetration at $t = 4.8$–5.5 s.

during field penetration. In the second category, the flux of Fe^{8+} and Mo^{12+} remains at the same level as before field penetration. In the third category, the flux of Mo^{13+}, C^{5+}, Cu^{17+} and W^{27+} decreases dramatically and is also sustained to the lowest level or even decreases further during field penetration. After the RMP is turned off ($t = 5.5$–6.1 s), the edge magnetic topology disappears, the flux of the edge impurity particles of He^{+}, Li^{2+}, O^{5+}, Fe^{8+} and Mo^{12+} decreases quickly, while that of Mo^{13+}, C^{5+}, Cu^{17+} and W^{27+} increases rapidly and soon arrives and is sustained at the highest level, which even exceeds the radiation level before RMP application. It could be found that the ions located more in the core region have a longer delay time to the highest level. In addition, due to the low concentration of heavy impurity in EAST plasma, $Z_{\rm eff}$ is mainly affected by light impurity [51]. By analyzing the impurity behavior in the plasma during the application of the RMP field (see figure 4), a significant increase in light impurity in the plasma edge is observed, resulting in an increase in $Z_{\rm eff}$, as shown in figure 2(*f*).

The differences in time evolution of different impurity ions during the periods of $I_{\rm RMP}$ ramp-up before field penetration, field penetration and RMP absent indicate that an effective layer is formed due to $n = 1$ RMP application, which is the so-called impurity screening layer. For the impurity ions located in the region between the plasma core and the layer, their flux decreases. However, for the impurity ions located between the layer and the plasma SOL region, their flux increases. Before field penetration, Mo^{13+} and C^{5+} ions are located at the edge of this screening layer while, after field penetration, Fe^{8+} and Mo^{12+} locate inside the screening layer. Since the radial distribution of impurity ions in the L-mode discharge dominated by RF heating is mainly determined by the ionization equilibration process, the ionization energy interval ($E_{\rm i}(Z-1) - E_{\rm i}(Z)$) of the impurity ion ($Imp^{Z+}$) can be used to roughly characterize the distribution. Firstly, the $T_{\rm e}$ range of the Imp^{Z+} is determined based on the $E_{\rm i}(Z-1) - E_{\rm i}(Z)$, and then the radial position (ρ) of the Imp^{Z+} is determined using the $T_{\rm e}$ profile (see figure 3(*b*)). Secondly, the spatial distribution of the Mo^{31+} ion measured by the space-resolved EUV spectrometer is used as a reference (see figure 7(*d*)), while considering the time-evolution behavior of impurity ions. Finally, the rough spatial distribution of each impurity species is obtained using the spline interpolation method, as shown in figure 5. Therefore, it can be found in figures 5(*a*) and (*b*) that the

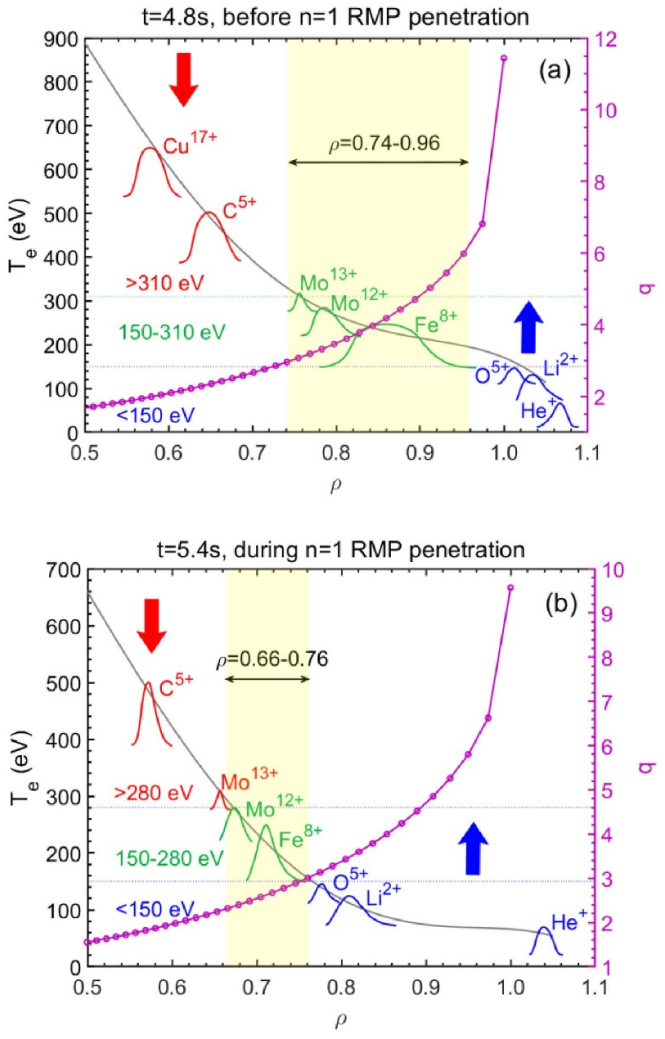

Figure 5. Radial profiles of the electron temperature (T_e) and safety factor (q) in the edge region (a) before RMP penetration ($t = 4.8$ s) and (b) during RMP penetration ($t = 5.4$ s). The yellow shaded area indicates the radial position where the RMP effect in both cases: $\rho = 0.74$–0.96 before RMP penetration, and $\rho = 0.66$–0.76 with RMP penetration.

screening layers of the impurity ions before and after RMP field penetration are located in the ranges 150–310 eV and 150–280 eV, respectively, i.e. the ρ are 0.74–0.96 and 0.66–0.76, respectively (see the yellow shaded areas in figures 5(a) and (b)). The possible reasons behind the significant differences in the behavior of these impurities after RMP field penetration will be explained in the discussion section of this paper.

3.2. Medium- and high-Z impurity decontamination in plasma core

Figure 6 analyzes the changes in the ratio of heavy impurity ion flux with and without the RMP field, $(\Gamma_{Imp}{}^{Z+})/(\Gamma_{Imp}{}^{Z+})_{w/o}$, to study the decontamination effects of RMP field strength on heavy impurities. And emission lines from highly ionized ions for W^{32+} (1283–1335 eV)

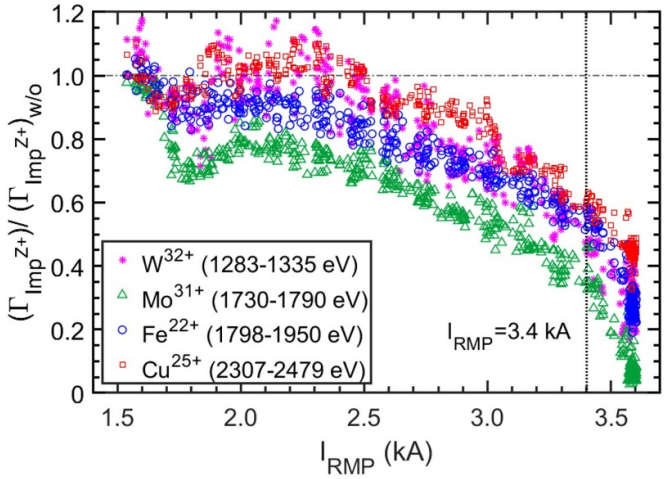

Figure 6. The ratio of the impurity ion flux with the RMP field to that without RMP field, $(\Gamma_{Imp}{}^{Z+})/(\Gamma_{Imp}{}^{Z+})_{w/o}$, for medium-Z (Fe and Cu) and high-Z (Mo and W) impurity ions in the core plasma, i.e. W^{32+} (1283–1335 eV), Mo^{31+} (1730–1790 eV), Fe^{22+} (1798–1950 eV) and Cu^{25+} (2307–2479 eV), as a function of the RMP coil current, I_{RMP}.

at 52.200 Å, Mo^{31+} (1730–1790 eV) at 127.868 Å, Fe^{22+} (1798–1950 eV) at 132.906 Å and Cu^{25+} (2307–2479 eV) at 111.186 Å are chosen. Initially, within 0.2 s of applying the RMP field (I_{RMP} from 1.5 kA to 1.7 kA), a rapid decrease in impurity ion flux is observed due to the changes in plasma confinement. Subsequently, the confinement performance of the plasma returns to stability, and results in a slow increase in ion flux (I_{RMP} from 1.7 kA to 2.0 kA). When the I_{RMP} increases from 2.0 kA to 3.4 kA, there is a significant decrease in impurity ion flux, leading to a decontamination effect of 30%–60%. Once I_{RMP} exceeds 3.4 kA, the decontamination effect becomes more significant, up to 60%–90%. The $(\Gamma_{Imp}{}^{Z+})/(\Gamma_{Imp}{}^{Z+})_{w/o}$ continues to decrease when I_{RMP} is sustained at 3.6 kA for 0.5 s. Among these impurities, the decontamination effect of Mo impurity is the most significant, followed by Fe and W impurities. This difference in decontamination effects does not appear to be directly related to the impurity atomic number.

3.3. Impurity density profiles

In addition, the vertical profiles of the chord-integrated line intensity of Li^{2+} at 135 Å, C^{5+} at the second order of 33.734 Å, W^{32+} at 52.2 Å, Mo^{31+} at 127.868 Å, Fe^{22+} at 132.906 Å and Cu^{25+} at 111.186 Å are measured by a pair of space-resolved EUV spectrometers [44, 45], as shown in figure 7. Due to the limited wavelength coverage of 30 Å for the space-resolved EUV spectrometer in one single discharge, the profiles are observed in three repeated discharges of #113745, #113746 and #113747 by wavelength scanning. The four timings in figure 7 are chosen as the same as those in figures 2 and 3, i.e. before RMP ($t = 2.8$ s), the onset of RMP penetration ($t = 4.8$ s), $m/n = 2/1$ LM with RMP ($t = 5.4$ s), and $m/n = 2/1$ tearing mode (TM) without RMP ($t = 5.8$ s),

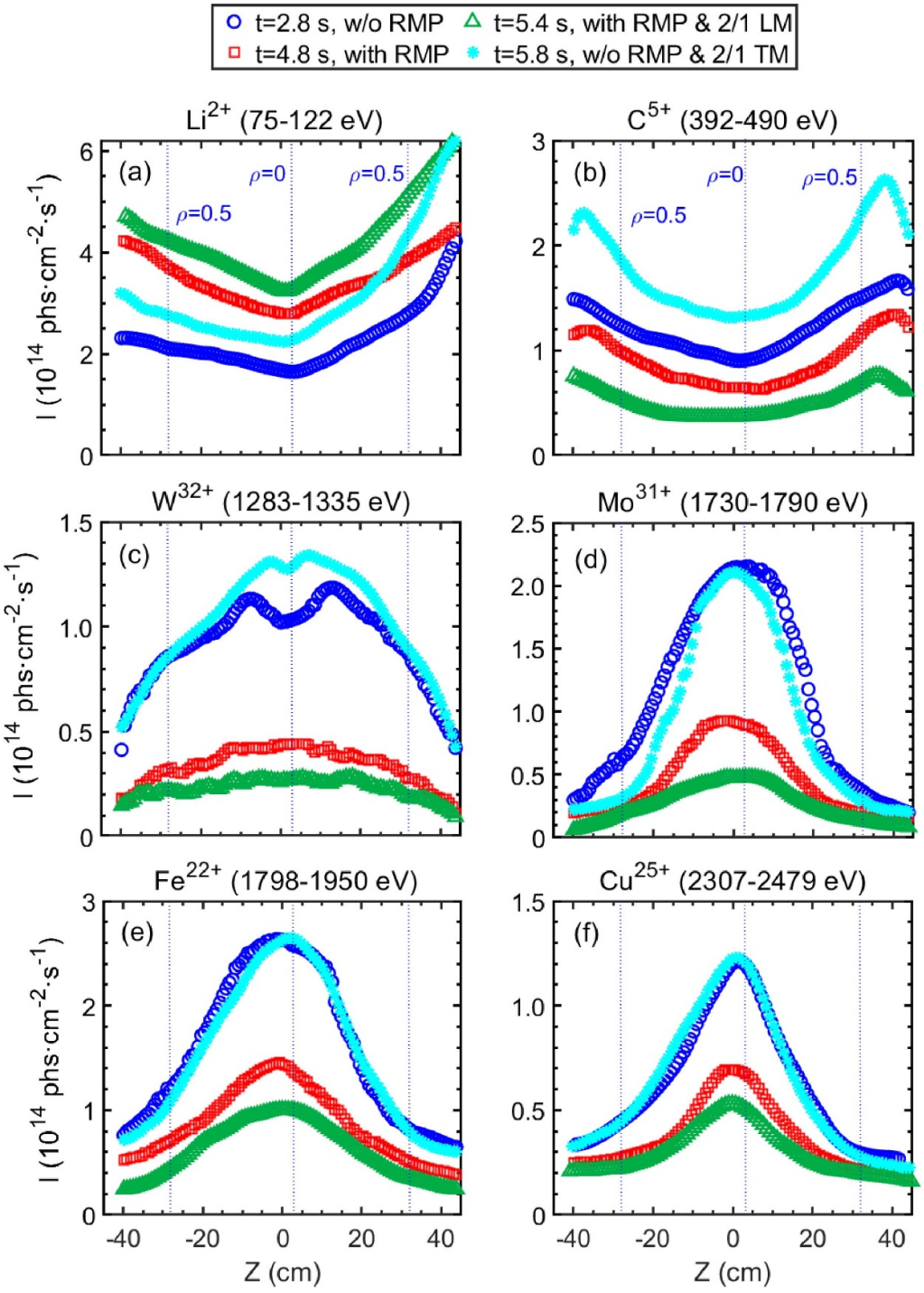

Figure 7. Vertical profiles of the chord-integrated line intensity of (*a*) Li^{2+} (75–122 eV) at 135 Å, (*b*) C^{5+} (392–490 eV) at the second-order line of 33.734 Å, (*c*) W^{32+} (1283–1335 eV) at 52.2 Å, (*d*) Mo^{31+} (1730–1790 eV) at 127.878 Å and (*e*) Fe^{22+} (1798–1950 eV) at 132.906 Å, and (*f*) Cu^{25+} (2307–2479 eV) at 111.186 Å. The timings of the measurements correspond to the timing before RMP application ($t = 2.8$ s), at the onset of RMP field penetration ($t = 4.8$ s), during field penetration ($t = 5.4$ s) and post RMP ($t = 5.8$ s), as indicated by the four vertical dashed lines in figure 2. The radial locations of $\rho = 0$ and $\rho = 0.5$ are indicated by vertical blue dotted lines.

respectively. And the radial locations of $\rho = 0$ and $\rho = 0.5$ are marked with blue vertical dotted lines. The results of these impurity profile distributions are consistent with the time evolution of impurity ion flux in figures 3 and 6, in which the spatial profiles of Li^{2+} increase significantly during application of the RMP field, while those of C^{5+}, W^{32+}, Mo^{31+}, Fe^{22+} and Cu^{22+} decrease and flatten, which is more particularly significant during 2/1 LM with RMP ($t = 5.4$ s). It is noted that the hydrogen-like lighter impurities Li^{2+} and C^{5+} can be observed to peak at the edge region of the plasma, e.g. the peaks of Li^{2+}

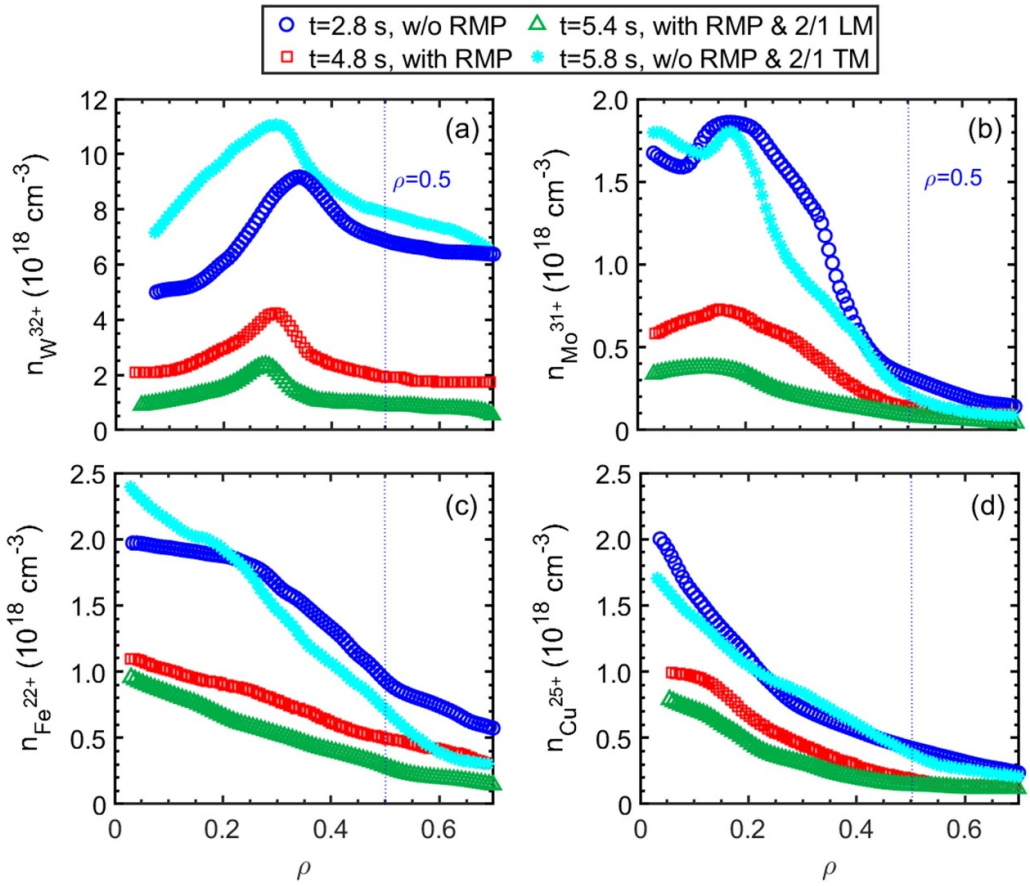

Figure 8. Density profiles of the impurity ions of (*a*) W^{32+} (1283–1335 eV), (*b*) Mo^{31+} (1730–1790 eV), (*c*) Fe^{22+} (1798–1950 eV) and (*d*) Cu^{25+} (2307–2479 eV). The radial locations of $\rho = 0.5$ are indicated by vertical blue dotted lines.

and C^{5+} are located at $\rho > 0.7$ and $\rho = 0.58$ after the RMP is switched off, respectively. With the increase in the ionization energy of the impurity ions (as shown in figures 7(*a*)–(*f*)), the intensity profile of the impurity line emission changes from hollow to peaking, e.g. hollow profiles with two peaks are observed for C^{5+} at $t = 4.8$ s and 5.8 s, and W^{32+} at $t = 2.8$ s and 5.8 s. The peak positions change at different timings.

Due to the influence of electron temperature and density, the distribution of impurity ions differs from the vertical intensity profile measured by space-resolved spectrometers. Therefore, based on the vertical intensity profile of impurity ion emission intensity measured by the space-resolved EUV spectrometer, combined with the Abel inversion and magnetic equilibrium fitting (EFIT) equilibrium code, the local emissivity of impurity ions can be reconstructed. The density distribution of impurity ions in different ionized states can thus be obtained by using the photon emission coefficient (PEC) of the emission line from the ADAS database [57]. Further details on impurity density calculations can be found in [44]. The density profiles are analyzed for W^{32+}, Mo^{31+}, Fe^{22+} and Cu^{25+} at $t = 2.8$ s, 4.8 s, 5.4 s and 5.8 s, as only the PEC data for these four impurity ions are available in the ADAS ADF15 database [52], as shown in figure 8. According to the density profile analysis, before the RMP application, the W impurity exhibits the highest concentrations, while the Mo, Fe and Cu impurities have similar concentrations. During the application of the RMP field, the decontamination effect of Mo is about 56% (see figure 8(*b*)), for Fe and W it is around 50% (see figures 8(*a*) and (*c*)), while for Cu it is ∼33%. Thus, the density profile findings are consistent with the results obtained from the impurity ion flux evolution (see figure 6), further indicating that the decontamination capability of RMP for heavy impurities does not appear to be directly correlated to the atomic numbers of the impurities.

3.4. The effect of $\Delta\Phi_{UL}$

From the above analysis, it can be found that the ability of RMP to decontaminate impurities is closely related to the I_{RMP}. Before RMP field penetration, with the increase in the I_{RMP}, the confinement performance of the plasma remains mostly unaffected by the I_{RMP}, while the decontamination effect on the impurity increases significantly. Therefore, a thorough analysis of the decontamination effects of RMP on impurities under different phase configurations is carried out to determine the effective range of RMP parameters that obtain impurity decontamination without compromising plasma confinement performance. We compare four exemplary pulse L-mode discharges with the same discharge conditions: (1) $\Delta\Phi_{UL} = 0°$ (#113745), (2) $\Delta\Phi_{UL} = 30°$ (#113751), (3) $\Delta\Phi_{UL} = 90°$ (#113749) and (4) $\Delta\Phi_{UL} = 270°$ (#113750). Furthermore, to further study the impact of RMP on impurity

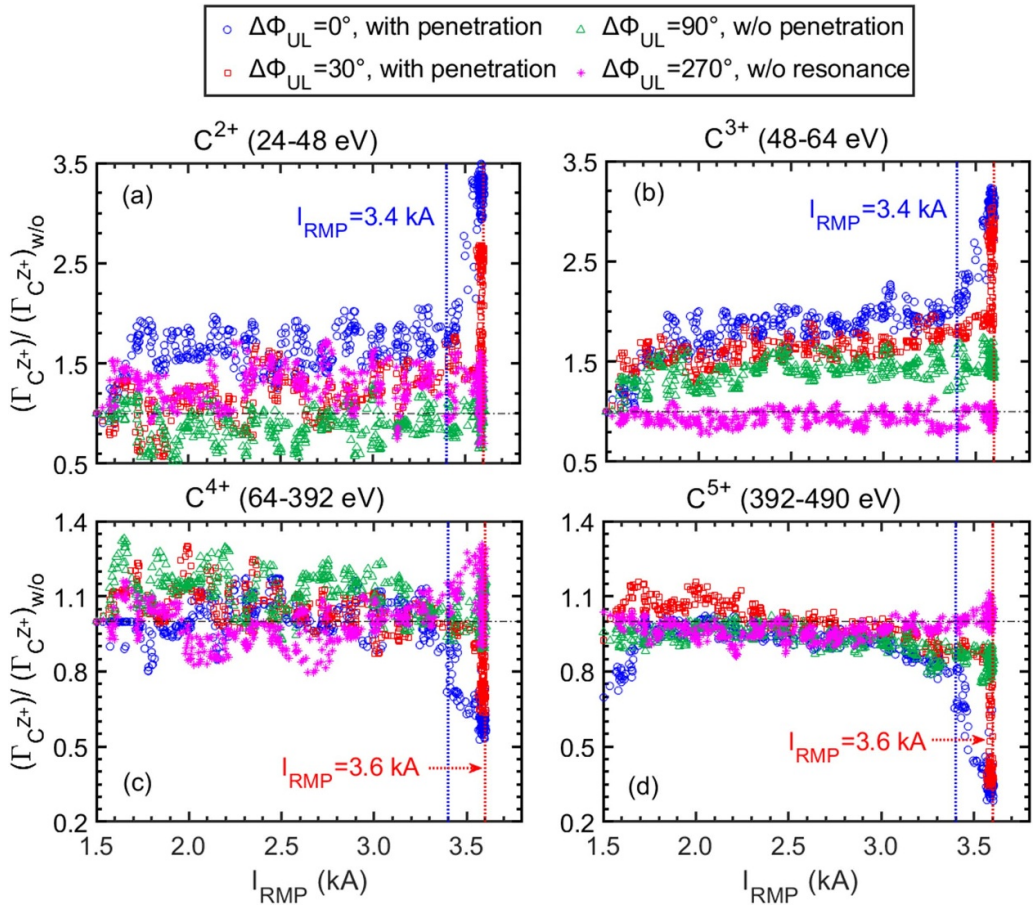

Figure 9. The ratio of the C ion flux with the RMP field to that without the RMP field, $(\Gamma_C{}^{Z+})/(\Gamma_C{}^{Z+})_{w/o}$, for (*a*) C^{2+} (24–48 eV) from the line of 459.630 Å, (*b*) C^{3+} (48–64 eV) from the line of 384.180 Å, (*c*) C^{4+} (64–392 eV) from the line of 40.268 Å and (*d*) C^{5+} (392–490 eV) from the line of 33.734 Å, as a function of the RMP coil current I_{RMP}. In four different RMP phases: $\Delta\Phi_{UL} = 0°$ with RMP penetration (blue hollow circles), $\Delta\Phi_{UL} = 30°$ with RMP penetration (red squares), $\Delta\Phi_{UL} = 90°$ without RMP penetration (green triangles) and $\Delta\Phi_{UL} = 270°$ without RMP resonance (magenta asterisks).

ions of different ionized states belonging to the same impurity, four distinct ionized states of C and Fe impurities, C^{2+} (24–48 eV) at 459.630 Å, C^{3+} (48–64 eV) at 384.180 Å, C^{4+} (64–392 eV) at 40.268 Å, C^{5+} (392–490 eV) at 33.734 Å, Fe^{8+} (151–234 eV) at 171.073 Å, Fe^{15+} (456–489 eV) at 360.758 Å, Fe^{17+} (1263–1358 eV) at 93.926 Å and Fe^{22+} (1798–1950 eV) at 132.906 Å, which are typical light and heavy impurities, respectively, that are due to have stronger spectral emission in the low-ionization and high-ionization stages than other impurity species in this work, are chosen, as shown in figures 9 and 10. According to the above study results, after RMP field penetration, for the impurity ions located in the region between the plasma core and the screening layer, their ion flux decreases abruptly. Meanwhile, for the impurity ions located between the screening layer and the plasma SOL region, their ion flux increases abruptly. The characteristics of the impurity ion flux evolution with I_{RMP} are observed in figures 9 and 10, when the phase differences of the RMP field are $\Delta\Phi_{UL} = 0°$ and 30°, there is penetration and penetration I_{RMP} is 3.4 kA and 3.6 kA, respectively (see the blue hollow circles and red squares in figures 9 and 10). However, no penetration is observed at $\Delta\Phi_{UL} = 90°$, only when the I_{RMP} is less than 3.6 kA (see the green triangles in figures 9 and 10). In addition, the C and Fe ions are almost constant at $\Delta\Phi_{UL} = 270°$ and I_{RMP} less than 3.6 kA, indicating that this phase is a non-resonant phase under this condition (see the blue magenta asterisks in figures 9 and 10). With the RMP application below the excitation threshold of the $m/n = 2/1$ LM, $(\Gamma_C{}^{Z+})/(\Gamma_C{}^{Z+})_{w/o}$ and $(\Gamma_{Fe}{}^{Z+})/(\Gamma_{Fe}{}^{Z+})_{w/o}$ increase slowly in the plasma edge region for C^{2+}, C^{3+} and Fe^{8+}, but there is a reduction in the plasma central region for C^{4+}, C^{5+}, Fe^{15+}, Fe^{17+} and Fe^{22+} (see the blue hollow circles, red squares and green triangles in figures 9 and 10). The evolutionary behavior of these impurity ion fluxes is consistent with figure 5(*a*). When $m/n = 2/1$, the LM becomes excited, and the impurity behavior of $(\Gamma_C{}^{Z+})/(\Gamma_C{}^{Z+})_{w/o}$ and $(\Gamma_{Fe}{}^{Z+})/(\Gamma_{Fe}{}^{Z+})_{w/o}$ at the edge and core is further amplified (see the blue hollow circles and red squares in figures 9 and 10), in which the decontamination effect of the Fe impurity is about 80%, while that of C impurity is about 70%. Therefore, when the RMP phase is between $\Delta\Phi_{UL} = 0°$ and 90°, and the I_{RMP} is lower than the penetration threshold, the decontamination effect of RMP on impurities also increases slowly with the increase in I_{RMP}, and the decontamination

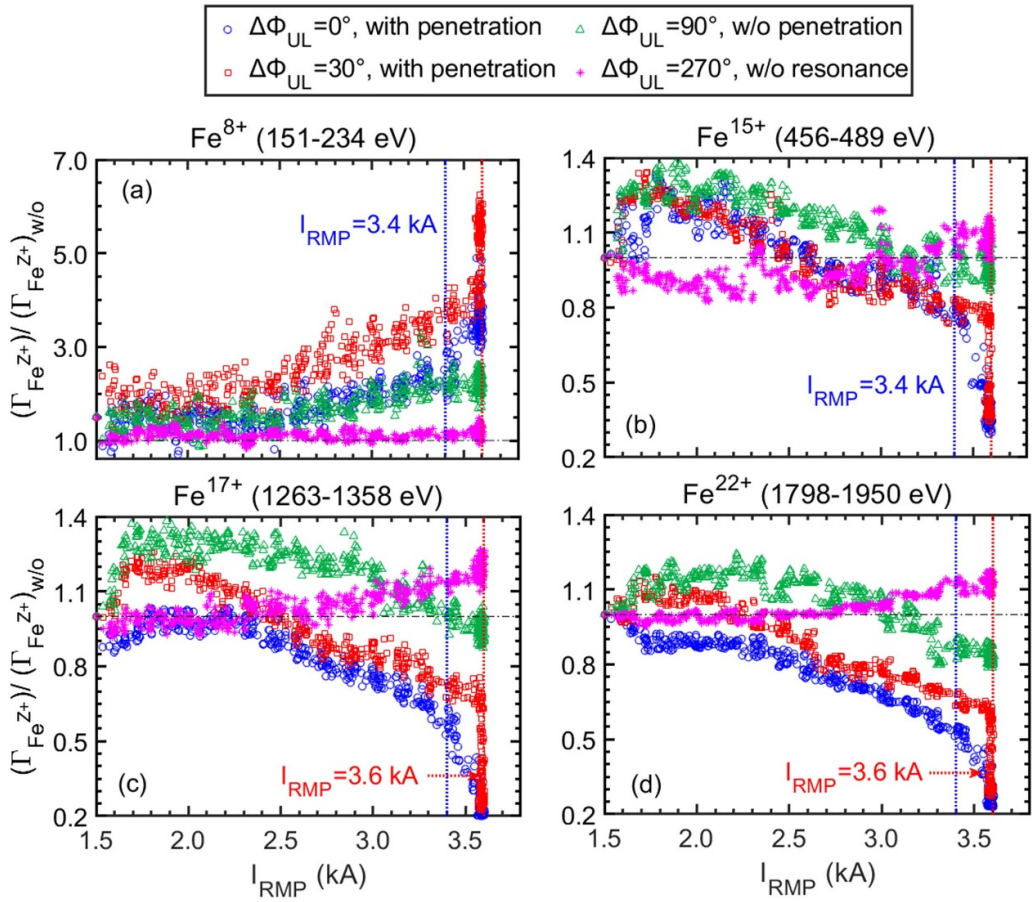

Figure 10. The ratio of the Fe ion flux with the RMP field to that without the RMP field, $(\Gamma_{Fe}{}^{Z+})/(\Gamma_{Fe}{}^{Z+})_{w/o}$, for (*a*) Fe^{8+} (151–234 eV) at 171.073 Å, (*b*) Fe^{15+} (456–489 eV) at 360.758 Å, (*c*) Fe^{17+} (1263–1358 eV) at 93.926 Å and (*d*) Fe^{22+} (1798–1950 eV) at 132.906 Å, as a function of the RMP coil current I_{RMP}. In four different RMP phases: $\Delta\Phi_{UL} = 0°$ with RMP penetration (blue hollow circles), $\Delta\Phi_{UL} = 30°$ with RMP penetration (red squares), $\Delta\Phi_{UL} = 90°$ without RMP penetration (green triangles) and $\Delta\Phi_{UL} = 270°$ without RMP resonance (magenta asterisks).

effect of heavy impurities seems to be better than that of light impurities.

4. Discussion

Based on the experimental results presented in figures 3, 4, 9 and 10, we observed that the T_e drops rapidly by 0.2 keV after RMP application, and subsequently remains stable. With the I_{RMP} increases, a distinct impurity screening layer is formed inside the last closed flux surface (LCFS) due to the alteration of the topology of the boundary magnetic field. This impurity screening layer induces significant opposite behavior in the impurity ion flux on both sides of the layer. After RMP field penetration, magnetic islands form on the $q = 2$ surface, altering the magnetic field configuration and enhancing the impurity transport in the plasma core [60]. This directly leads to a reduction in impurity flux in the plasma core. As a result, the impurity screening layer shifts toward the plasma core and its width decreases, which leads to a decrease in the impurity ion flux near the interior region of the original screening layer. Therefore, we observed, in the experiment, that when the RMP field penetrates, the impurity flux of the Mo^{13+} ion changes from increasing to decreasing, and the increase in impurity ion flux at the edge has a delay of about 1 s. Furthermore, the impact of the impact of the neoclassical toroidal viscosity (NTV) effect on impurity behavior before and after RMP field penetration is analyzed [33, 61]. Modeling results with NTVTOK suggest that after RMP field penetration, the impurity ion flux of Li^{2+} increases, while the flux of C^{5+} decreases. This indicates that NTV effects may be one of the main reasons preventing impurity transport from the plasma edge to the core. On the other hand, previously published experimental results show that the impurity concentrations of C and Fe have a significant reduction when the ELM is suppressed during H-mode discharge, and simulations using EMC3 and STRAHL show that the decrease in impurity ion concentration is attributed to the increased diffusion and the decreased convection of impurity ions [62, 63].

According to the ionization energy of impurity ions, the T_e profile and the impurity ion flux changes in figure 4, the region where the RMP field has an effect before and after RMP field penetration can be determined in figures 5(*a*) and (*b*), where the yellow shaded area is the screening layer region, i.e. ρ = 0.74–0.96 and 0.66–0.76 before and during field penetration, respectively. When the RMP field penetrates, it

is found that a magnetic island is formed at the position of $\rho \sim (0.61–0.67)$, while the impurity screening layer is locating in the $\rho = 0.66–0.76$ region, with about 40% overlap. Part of the magnetic island is located within the screening layer, which indicates that formation of the magnetic island may promote the movement of the impurity screening layer toward the plasma core region. The estimated peak position of C^{5+} ion distribution is $\rho \approx 0.64$ and 0.56, while it is measured in figure 7(*a*) as 0.62 and 0.55, respectively. The difference between the two is very small, indicating that the uncertainty caused by impurity transport in this case can be ignored. In addition, the changes in the flux of C and Fe impurity ions in different ionized stages in figures 9 and 10 are consistent with the RMP-affected region in figure 5. Therefore, the radial region where the RMP field has an effect during the different n RMP field applications in impurity decontamination experiments in L-mode discharge can be determined by tracking the evolution of abundant intrinsic impurity ion emissions in EAST plasma. In L-mode discharge, when the $n = 1$ RMP penetrates, it mainly occurs on the magnetic surface of $q = 2$, where ρ is larger than 0.5. The radial magnetic response perturbations B_r are closely related to the plasma parameters, i.e. B_T and q_{95} [54]. However, the inversion of impurity flux predominantly takes place near this position and is closely associated with the width of the magnetic island. Although, in H-mode discharge, it may be necessary to consider the impact of the transport coefficient in the pedestal region on the distribution of impurity ions to determine the radial region range of the RMP field, this information is still useful for evaluating the suitable range of RMP parameters and ensures the smooth progress of the experiment. Furthermore, W impurity lines are being carefully identified in EAST; the radial position range of the RMP response can thus be estimated using the evolution behavior of W impurity ion emission in different ionized stages in H-mode discharges.

In addition, the evolution behavior of C and Fe impurities under four different RMP phase difference configurations demonstrates significant differences in the decontamination effects on impurity ions with respect to different RMP phase configurations. This suggests that the response of the RMP field (resonant and non-resonant components) in different RMP phase configurations plays a crucial role in the decontamination effect [32]. To further analyze and understand the impact of plasma response on impurity decontamination under these four phase configurations, the RMP spectrum, taking into account plasma response, will be simulated using the MARS-Q code in the future [64].

5. Summary

High-Z impurity accumulation suppression in core plasma is frequently observed in EAST ELM mitigation experiments by using RMP coils. To study the individual effects of the RMP field on impurity transport, in this work, the edge intrinsic impurity behavior with application of $n = 1$ RMP in EAST L-mode plasma is experimentally studied for the first time. The time-evolution behavior of the particle flux of He^{+}, Li^{2+}, C^{2+}–C^{5+}, O^{5+}, Fe^{8+}, Fe^{15+}, Fe^{17+}, Fe^{22+}, Cu^{17+}, Mo^{12+}, Mo^{13+} and W^{27+} ions changes with increasing I_{RMP} is clearly observed. It is found that an impurity screening layer is formed inside the last closed flux surface with the increase in I_{RMP}, and the impurity ion flux between this layer and the plasma core decreases, e.g. C^{4+}, C^{5+}, Cu^{17+}, W^{27+}, Fe^{15+}, Fe^{17+} and Fe^{22+}, while it increases in other regions, e.g. He^{+}, Li^{2+}, C^{2+}, C^{3+}, O^{5+}, Fe^{8+}, Mo^{12+} and Mo^{13+}. Based on the ionization energy of impurity ions, the T_e profile and the time-evolution behavior of impurity ion flux, it can be determined that the screening layer is mainly located at $\rho = 0.74–0.96$. When the I_{RMP} exceeds the penetration threshold, the screening layer moves to $\rho = 0.66–0.76$, and this opposite impurity ion flux behavior is further strengthened dramatically, in which the impurity ion flux in the plasma edge region decreases with a delay of about 1 s. Before RMP field penetration, the T_e drops slightly within 0.2 s at the initial RMP application and then remains constant. Therefore, this change in impurity ion flux is mainly due to the screening effect generated by the RMP field at the edge. However, after RMP field penetration, impurity transport in the core plasma is due to the formation of 2/1 LM on the $q = 2$ surface. Meanwhile, before RMP field penetration, the decontamination effect of heavy impurities (Fe, Cu, Mo and W) can reach 30% to 60%, of which Mo impurities are the most significant, followed by Fe and W impurities, and for light impurity, C is about 27%. During RMP field penetration, the decontamination effect of heavy and light impurity can be increased to 60%–90% and 70%, respectively. This seems to indicate that the decontamination effect is not significantly affected by the impurity atomic number, but the decontamination effect of heavy impurity is better than that of light impurity. Furthermore, the decontamination effects of C and Fe impurities under four different RMP phase configurations show that the decontamination effect of the RMP field on impurity ions is closely related to the resonance effect and the strength of the RMP field. Therefore, these results not only extend the understanding that RMP reduces the concentration of impurities in the plasma core, they show that the method used in this work to determine the impurity screening layer generated by the RMP field is critical for future impurity and ELM control using RMP fields. In the near future, other potential physical mechanisms for the decontamination effects of RMP will continue to be analyzed based on the experimental results. Identification of low-ionized W ions (W^{4+}–W^{20+}) will be reconfirmed and utilized in the future analysis. In addition, a statistical study on the edge/pedestal light and heavy impurity transport with the effects of RMP fields will be carried out using a combination of high-performance edge impurity diagnostics and a core–edge coupling impurity transport study.

Acknowledgments

The authors are grateful to Dr Tao Zhang and Dr Zhen Zhou who helped to analyze the poloidal reflectometer data, and Dr Qing Zang, Dr Jian Zhou and Dr Hailin Zhao who provided electron temperature data. This work was supported

by the National MCF Energy R&D Program (Grant No. 2022YFE03180400), National Natural Science Foundation of China (Grant No. 12322512), and Chinese Academy of Sciences President's International Fellowship Initiative (PIFI) (Grant Nos. 2024PVA0074 and 2020VMA0001).

ORCID iDs

Wenmin Zhang https://orcid.org/0009-0000-9980-6765
Yunxin Cheng https://orcid.org/0000-0002-9195-2757
Darío Mitnik https://orcid.org/0000-0003-0193-0958
Youwen Sun https://orcid.org/0000-0002-9934-1328
Yuqi Chu https://orcid.org/0000-0002-7379-0117
Haiqing Liu https://orcid.org/0000-0001-6892-358X

References

[1] Doerner R.P., Baldwin M.J., De Temmerman G., Hanna J., Nishijima D., Roth J., Schmid K., Tynan G.R. and Umstadter K. 2009 *Nucl. Fusion* **49** 035002
[2] Philipps V. 2011 *J. Nucl. Mater.* **415** S2–9
[3] Pütterich T., Fable E., Dux R., O'Mullane M., Neu R. and Siccinio M. 2019 *Nucl. Fusion* **59** 056013
[4] Nunes I. 2016 *Plasma Phys. Control. Fusion* **58** 014034
[5] Burrell K.H. *et al* 1989 *Plasma Phys. Control. Fusion* **31** 1649
[6] Lipschultz B. *et al* 2007 *Nucl. Fusion* **47** 1189
[7] Jackson G.L., Taylor T.S. and Taylor P.L. 1990 *Nucl. Fusion* **30** 2305
[8] Zuo G.Z., Hu J.S., Zhen S., Li J.G., Mansfield D.K., Cao B., Wu J.H. and Zakharov L.E. 2012 *Plasma Phys. Control. Fusion* **54** 015014
[9] Hu J.S. *et al* 2016 *Nucl. Fusion* **56** 046011
[10] Xu W. *et al* 2021 *Phys. Scr.* **96** 124034
[11] Bortolon A. *et al* 2020 *Nucl. Fusion* **60** 126010
[12] Lunsford R. *et al* 2022 *Nucl. Fusion* **62** 186021
[13] Sips A.C.C. and Gruber O. 2008 *Plasma Phys. Control. Fusion* **50** 024028
[14] Cui Z.Y. *et al* 2013 *Nucl. Fusion* **53** 093001
[15] Angioni C., Sertoli M., Bilato R., Bobkov V., Loarte A., Ochoukov R., Odstrcil T., Pütterich T. and Stober J. 2017 *Nucl. Fusion* **57** 056015
[16] Zhang L. *et al* 2017 *Nucl. Mater. Energy* **12** 774–8
[17] Valisa M. *et al* 2011 *Nucl. Fusion* **51** 033002
[18] Czarnecka A. *et al* 2012 *Plasma Phys. Control. Fusion* **54** 074013
[19] Sertoli M., Odstrcil T. and Angioni C. 2015 *Nucl. Fusion* **55** 113029
[20] Hender T.C. *et al* 2016 *Nucl. Fusion* **56** 066002
[21] Lippmann S., Finkenthal M., Moos H.W., McCool S.C. and Wootton A.J. 1991 *Nucl. Fusion* **31** 2131
[22] Ghendrih P. *et al* 2002 *Nucl. Fusion* **42** 1221
[23] Finken K.H. *et al* 1995 *J. Nucl. Mater.* **220** 448–51
[24] Evans T.E. *et al* 2005 *J. Nucl. Mater.* **337** 691–6
[25] Liang Y. *et al* 2007 *Phys. Rev. Lett.* **98** 265004
[26] Jeon Y.M. *et al* 2012 *Phys. Rev. Lett.* **109** 035004
[27] Sun Y. *et al* 2016 *Nucl. Fusion* **57** 036007
[28] Suttrop W. *et al* 2011 *Phys. Rev. Lett.* **106** 225004
[29] Breton C. *et al* 1991 *Nucl. Fusion* **31** 1774
[30] Telesca G., Crombé K., Tokar M., Unterberg B., Verdoolaege G., Zagorski R. and Van Oost G. 2005 *J. Nucl. Mater.* **337** 361–5
[31] Victor B.S. *et al* 2020 *Plasma Phys. Control. Fusion* **62** 095021
[32] Sun Y. *et al* 2021 *Nucl. Fusion* **61** 106037
[33] Chang Y.Y. *et al* 2023 *Phys. Plasmas* **30** 122301
[34] Schmitz O. *et al* 2016 *Nucl. Fusion* **56** 106011
[35] Hinson E.T. *et al* 2020 *Nucl. Fusion* **60** 054004
[36] Sun Y., Liang Y. and Liu Y.Q. 2016 *Phys. Rev. Lett.* **117** 115001
[37] Wang L. *et al* 2021 *J. Fusion Energy* **40** 1–21
[38] Dai S.Y., Zhang H.M., Lyu B., Sun Y.W., Jia M.N., Feng Y., Wang Z.X. and Wang D.Z. 2020 *Plasma Phys. Control. Fusion* **63** 025003
[39] Zhang L. *et al* 2015 *Rev. Sci. Instrum.* **86** 123509
[40] Zhang L. *et al* 2019 *Nucl. Instrum. Methods Phys. Res.* A **916** 169–78
[41] Xu Z. *et al* 2021 *Nucl. Instrum. Methods Phys. Res.* A **1010** 165545
[42] Li L. *et al* 2021 *Plasma Sci. Technol.* **23** 075102
[43] Zhang W.M. *et al* 2022 *Phys. Scr.* **97** 045604
[44] Cheng Y.X. *et al* 2022 *IEEE Trans. Plasma Sci.* **50** 691–9
[45] Cheng Y.X. *et al* 2022 *Rev. Sci. Instrum.* **93** 123501
[46] Cheng Y.X. *et al* 2023 *Nucl. Instrum. Methods Phys. Res.* A **1057** 168714
[47] Song Y.T. *et al* 2023 *Sci. Adv.* **9** eabq5273
[48] Liu H.Q. *et al* 2014 *Rev. Sci. Instrum.* **85** 11D405
[49] Liu X., Zhao H.L., Li Y., Li E.Z., Han X., Domier C.W., Luhmann N.C., Ti A., Hu L.Q. and Zhang X.D. 2014 *Rev. Sci. Instrum.* **85** 093508
[50] Duan Y.M., Hu L.Q., Mao S.T., Xu P., Chen K., Lin S., Zhong G., Zhang J., Zhang L. and Wang L. 2011 *Plasma Sci. Technol.* **13** 546
[51] Chen Y.J., Wu Z.W., Gao W., Ti A., Zhang L., Jie Y., Zhang J., Huang J., Xu Z. and Zhao J. 2015 *Rev. Sci. Instrum.* **86** 023509
[52] Zhou Z. *et al* 2021 *Plasma Sci. Technol.* **23** 075101
[53] Urbanczyk G. *et al* 2020 *Nucl. Fusion* **60** 126003
[54] Wang H.H. *et al* 2020 *Nucl. Fusion* **60** 126008
[55] Zhang Y. *et al* 2021 *Nucl. Fusion* **61** 096028
[56] Behringer K., Summers H.P., Denne B., Forrest M. and Stamp M. 1989 *Plasma Phys. Control. Fusion* **31** 2059
[57] The atomic data and analysis structure (ADAS) is an interconnected set of computer codes and data collections for modelling the radiating properties of ions and atoms in plasmas (available at: https://open.adas.ac.uk/)
[58] Klapisch M., Schwob J.L., Fraenkel B.S. and Oreg J. 1977 *Josa* **67** 148–55
[59] Bar-Shalom A., Klapisch M. and Oreg J. 2001 *J. Quant. Spectrosc. Radiat. Transfer* **71** 169–88
[60] Hender T.C. *et al* 1992 *Nucl. Fusion* **32** 2091
[61] Sun Y., Li X., He K. and Shaing K.C. 2019 *Phys. Plasmas* **26** 072504
[62] Dai S.Y., Zhang H.M., Lyu B., Wang L., Feng Y., Wang Z.X. and Wang D.Z. 2020 *J. Plasma Phys.* **86** 815860303
[63] Vogel G. *et al* 2021 *J. Plasma Phys.* **87** 905870213
[64] Liu Y., Kirk A. and Sun Y. 2013 *Phys. Plasmas* **20** 042503